Geometric and Electronic Structures of Multiple-Decker One-End Open Sandwich Clusters: $Eu_n(C_8H_8)_n^-$ ($n = 1-4$)

Ryuta Takegami,[†] Natsuki Hosoya,[†] Jun-ichi Suzumura,[†] Atsushi Nakajima,[†,‡] and Satoshi Yabushita*[,†]

Department of Chemistry, Faculty of Science and Technology, Keio University, 3-14-1 Hiyoshi, Kohoku-ku, Yokohama 223-8522, Japan, and CREST, Japan Science and Technology Agency (JST), c/o Department of Chemistry, Keio University, Yokohama 223-8522, Japan

Received: November 12, 2004; In Final Form: January 18, 2005

We have measured the photoelectron spectra of the multiple-decker 1:1 sandwich clusters of $Eu_n(COT)_n^-$ ($n = 1-4$; COT = 1,3,5,7-cyclooctatetraene), synthesized in the gas phase, and studied theoretically the bonding scheme, charge distribution, valence orbital energies, and photodetachment energies. We calculated the ground electronic state X^- and the first excited electronic state A^-, both of which have strong ionic bonding and a characteristic charge distribution. Moreover, we found that the valence orbital energies of Eu (6s) and COT (L_δ) depend strongly on cluster size and their positions in the clusters. With the calculated vertical detachment energies for these valence orbitals, we assigned the peaks in the experimental photoelectron spectra and analyzed the origin of their interesting behavior by employing simple *point charge models*. From these analyses, it became clear that the characteristic behavior of the spectra is due to the strong ionic bonding and the charge distribution. In addition, using the point charge models, we estimated the vertical detachment energies of the one-dimensional polymer $[Eu(COT)]_\infty^-$.

1. Introduction

The advent of the laser vaporization synthesis method in the 1980s[1−3] and the successive development of the technique during the last 10 years[4,5] have enabled us to generate various kinds of novel clusters without environmental factors such as oxidation or reduction of the products. Moreover, considerable experimental and theoretical efforts have recently revealed their characteristic physical and chemical properties, which have been anticipated for the application to new nanostructured materials. In this regard, our group has reported the preparation of multiple-decker sandwich clusters, in which metal atoms and organic ligands are alternately stacked one-dimensionally.[5] Typical examples for the sandwich clusters are combinations of vanadium (V) atoms and benzene (Bz) molecules and those of lanthanide (Ln) atoms and cyclooctatetraene (COT) molecules.

In the case of the V−Bz sandwich clusters, many experimental and theoretical studies in the past decade have clarified their geometric and electronic structures.[6−13] For instance, we have studied the bonding scheme and ionization energies both experimentally and theoretically and have made it clear that $V_n(Bz)_{n+1}$ have covalent bonding due to the charge-transfer interaction between the Bz lowest unoccupied molecular orbitals (LUMOs) and the d_δ orbitals of V. This builds up the one-dimensional quasi-band structure.[6−8] Following these earlier studies, Pandey and co-workers performed density functional theory (DFT) calculations for the neutral and anion V−Bz clusters and obtained the electron affinities, ionization energies, and ground-state spin multiplicities.[9,10] Broyer and co-workers determined the permanent dipole moment of $V(Bz)_2$ and V(Bz) using molecular beam deflection experiments in an inhomogeneous electric field and theoretical calculations.[11,12] They reported that the $V(Bz)_2$ sandwich cluster has no dipole moment because of its symmetrical structure. They also reported that the one-end open sandwich cluster of V(Bz), somewhat curiously, has a negligible dipole moment. It is reasonable, however, if the dominantly prepared stable structure is weakly bound by a long-range van der Waals force and, thus, has no charge polarization in the cluster. Recently, Miyajima et al. measured the magnetic moments of $V_n(Bz)_{n+1}$ by a molecular beam magnetic deflection method with a Stern−Gerlach magnet and found a monotonic increase of the magnetic moment with the cluster size.[13]

Over the past half a century, a lot of studies have been conducted in the condensed phase organometallic chemistry with rare earth metals, as reviewed, for example, by Schumann et al.[14] Particularly, the complex of Ln and COT was first isolated by Hayes and Thomas in 1969.[15] Since then, there have been many studies of their synthesis,[16−19] geometric structure, and chemical properties.[19−24] Their bonding scheme has been recognized as fairly ionic, and their maximum size has been reported as several layers. On the other hand, there have been only a limited number of theoretical works concerning Ln−COT complexes. Dolg and co-workers investigated the geometric and electronic structures of the $Ln(COT)_2$ (Ln = Ce, Nd, Tb, and Yb), which are the smallest unit of $Ln_n(COT)_m$ sandwich clusters.[25−28] They reported that $Ln(COT)_2$ have D_{8h} symmetry and, as a first approximation, consist of Ln^{3+} positive central metal ions pinched with two $COT^{1.5-}$ rings.

It is only recently that gas-phase experimental works have been performed on Ln−COT complexes with the laser vaporization synthesis method. Kurikawa et al. measured the electron binding energies and the ionization energies of larger $Ln_n(COT)_m$ (Ln = Ce, Nd, Eu, Ho, Er, and Yb) with photoelectron

* To whom correspondence should be addressed. E-mail: yabusita@chem.keio.ac.jp. Fax: +81-45-566-1697.
[†] Keio University.
[‡] CREST, Japan Science and Technology Agency.

10.1021/jp044806n CCC: $30.25
Published on Web 02/25/2005

spectroscopy.[29,30] On the basis of the experimental results and the theoretically predicted charge distribution of $Ln(COT)_2$, they suggested that the $Ln_n(COT)_m$ sandwich clusters also have a strong ionic bonding owing to the electron transfer from Ln to COT. Miyajima et al. also discussed the charge distribution of Ln−COT clusters by a chemical probe method with Na atoms as electron donors.[31] Recently, our group has succeeded in synthesizing larger Eu−COT sandwich clusters, named as sandwich nanowires, in the gas phase using a combination of laser vaporization techniques and molecular beam methods.[32] In contrast to $V_n(Bz)_m$, which was limited to seven layers, Eu−COT sandwich nanowires were formed with up to one-dimensional 18 layers (about 8 nm overall length) which stimulated theoretical investigation.

In this work, we report a combined experimental and theoretical study on the geometric and electronic structures of one-end open 1:1 sandwich clusters of $En_n(COT)_n^-$ ($n = 1-4$), because they are considered to be important intermediates in the sequential formation step of the larger Eu−COT sandwich nanowires and their photoelectron spectra show a characteristic dependence on the cluster size.[32] In addition, such a study is essential to understand the properties of the larger cluster and other $Ln_n(COT)_m$ compounds.

In section 2, we describe experimental methods for photoelectron spectroscopy, and in section 3, we describe computational details. In section 4, we first present the experimental photoelectron spectra which show interesting cluster size dependencies. Next, we theoretically give optimized geometries and their charge distribution for two different electronic states, and discuss the characteristic behavior of valence orbital energies of the Eu and COT portions which exhibit strong dependency on the cluster size and the relative positions. We assign the experimental photoelectron spectra in comparison with the DFT calculations and also with the spectra of Ba−COT. Furthermore, we reveal the physical origin of the characteristic behavior of the valence orbital energies with simple *point charge models*. Using the point charge models, we easily estimate the vertical detachment energies (VDEs) of the one-dimensional polymer $[Eu(COT)]_\infty^-$. Finally, we depict one-dimensional potential curves, based on the linear synchronous transit (LST) paths,[33] to investigate the energetic relations among the anion and neutral clusters.

2. Experimental Section

Details of the experimental setup were previously described elsewhere.[34] Briefly, $Eu_n(COT)_n$ complexes were synthesized via the gas-phase reaction between laser-vaporized Eu atoms and COT molecules. After the growth of the cluster in a channel, the neutral clusters of Eu−COT were photoionized with an ArF excimer laser (6.42 eV) and were mass-analyzed with a reflectron time-of-flight (TOF) mass spectrometer. The photoelectron spectra of the $Eu_n(COT)_n$ cluster anions were measured using a magnetic bottle TOF photoelectron spectrometer.[35] The $Eu_n(COT)_n$ clusters were generated by the laser vaporization method mentioned above, and only the cluster anions were accelerated to 1500 eV. After being decelerated, the mass-selected cluster anions were photodetached with the third harmonic (355 nm; 3.49 eV) or the fifth harmonic (213 nm; 5.83 eV) of a Nd^{3+}:YAG laser. When the photoelectron spectra of barium (Ba)−COT cluster anions were measured to compare with those of Eu−COT, the same experimental procedures were applied using a Ba rod instead of an Eu rod. The photoelectron signal was typically accumulated to 30 000−50 000 shots. The energy resolution was typically about 50 meV full width at half-maximum at a 1-eV electron energy. The energy of the photoelectron was calibrated by measuring the photoelectron spectra of Au^-.[36] The laser power for photodetachment was in the range of 3−5 mJ/cm^2, and the spectrum shape exhibited no laser-power-dependent processes.

3. Computational Method

All the DFT calculations were carried out with the B3LYP functionals[37] built in the Gaussian 98 program package.[38] Throughout this paper, bond lengths are given in angstroms (Å) and energies are given in electronvolts (eV). A molecular axis (z axis) is defined as a line passing through Eu and the center of gravity of the COT ligand. The eight π molecular orbitals on a COT ligand are denoted, based on their symmetries, as nondegenerate L_σ; doubly degenerate L_π, L_δ, and L_ϕ; and nondegenerate L_γ; therefore, the valence electronic configurations of COT^{2-} and COT^- are $L_\sigma^2L_\pi^4L_\delta^4$ and $L_\sigma^2L_\pi^4L_\delta^3$, respectively. The geometric structure of the aromatic ground-state COT^{2-} is D_{8h}. For COT^-, the minimum energy structure has been reported as D_{4h} with alternating C−C bond lengths.[39,40] Valence electronic configurations of the ground states of Eu^{2+}, Eu^+, and Eu are $4f^7$, $4f^76s^1$, and $4f^76s^2$, respectively, in which the 4f electrons always have a half-filled shell structure with a corelike character.

As reported previously,[29,30] the charge distribution for the Eu−COT clusters consists of Eu^{2+} cations and COT^{2-} anions. On the basis of the above-mentioned configurations of Eu, which have a corelike character of $4f^7$, and the charge distribution model of $Eu_n(COT)_n$, we applied three different combinations of basis sets and effective core potentials (ECPs): 4f CORE-A, 4f CORE-B, and 4f VALENCE. In 4f CORE-A, we chose the 4f core ECP and (7s6p5d)/[5s4p3d] basis set of the Stuttgart/Cologne group[41] for Eu and the D95 basis set[42] for COT. In 4f CORE-B, to see the effect of polarization and diffuse functions for COT^{2-}, the D95 basis was replaced by the 6-31+G(d) basis set.[43] In 4f VALENCE, we employed the 4f valence ECP and (12s11p10d8f)/[5s5p4d3f] basis set of the Stuttgart/Cologne group for Eu[41] and 6-31+G(d) for COT.

4. Results and Discussions

4.1. Photoelectron Spectra. We have measured photoelectron spectra of $Eu_n(COT)_n^-$ ($n = 1-4$) to gain detailed information about their electronic structure. Figures 1 and 2 show the spectra with the third harmonic (355 nm; 3.49 eV) and the fifth harmonic (213 nm; 5.83 eV) of a Nd^{3+}:YAG laser, respectively. In the spectra, the horizontal axis corresponds to the electron binding energy, E_b, defined as $E_b = h\nu - E_k$, where E_k is the kinetic energy of the photoelectron.

In Figure 1, we find two significant peaks: the first one shifts to the higher energy side with the cluster size (M peak), and the second one is almost independent of the cluster size (C(1) peak). In the spectra of $n = 2$, we also observe the weak hot band around the binding energy of 1.0 eV (H peak). In Figure 2, we observe successive peaks where the number of peaks increases according to the cluster size (C(i) peak). To assign the photoelectron spectra and explain the physical origin of their characteristics, we will discuss the theoretical studies on geometric and electronic structures of $Eu_n(COT)_n^-$ in the following sections.

4.2. Optimized Geometry, Charge Distribution, and Localized Molecular Orbitals. Figure 3 shows the formal charge distribution, together with the optimized distances between the metal and the center of gravity of the COT carbon ring. The formal charges are easily determined by counting the number

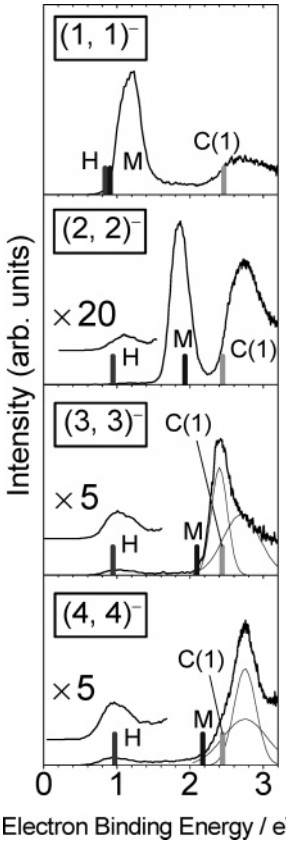

Figure 1. Experimental photoelectron spectra for $(n, n)^-$ ($n = 1-4$) at the photon energy of 355 nm (3.49 eV) and calculation results with ΔDFT shown by vertical lines. Symbols M and C(1) represent the M and C(1) peaks from the X^- state, and symbol H denotes the H peak from the A^- state as described in section 4.3. The M peak shifts to the higher energy side with the cluster size, and the C(1) and H peaks are almost independent of the cluster size.

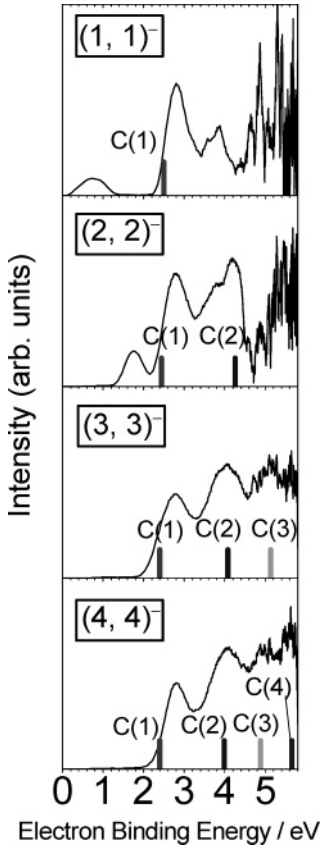

Figure 2. Experimental photoelectron spectra for $(n, n)^-$ ($n = 1-4$) at the photon energy of 213 nm (5.83 eV) and calculation results with vertical lines, which are obtained by Koopmans' theorem with the UHF orbital energies. Symbol C(i) stands for the detachment from each COT(i) in the X^- state as described in section 4.3. The number of C(i) peaks increases according with the cluster size.

of electrons among the valence orbitals, namely, the 6s and L_δ orbitals, because each orbital is well localized on Eu or COT, as discussed later. In this figure, the black, dotted, and white circles denote neutral, +1, and +2 charged metals, and dotted and white plates denote −1 and −2 charged COT ligands, respectively. As lower-lying electronic states, we found two different doublet states (with 4f core ECP), which we call the X^- and A^- states. The A^- state arises by a one-electron transfer from the left-end COT^{2-} to the right-end Eu^+ ion in Figure 3a. Interestingly, our computational results showed that the exposed metal atom carried charges of +1 and 0 in the X^- and A^- states, respectively, and the COT^- ligand was always the exposed ligand in the A^- state, as shown in Figure 3. Moreover, the A^- state was an excited state, namely, higher than the X^- state in energy, in all the cluster sizes studied. Additional details will be discussed in section 4.5.

The optimized distances between Eu and COT in Figure 3 show a very small basis set dependency; namely, the maximum deviation between CORE-A and CORE-B was about 0.03 Å for $n = 1-3$. The geometry optimization with 4f VALENCE performed only for $n = 1$ shows a slightly larger deviation yet less than 0.1 Å in the distance between Eu and COT.

The geometries of the X^- and A^- states are specified with two kinds of distances, r_a and r_b, as shown in the lower part of Figure 3. r_a is the bond distance between an Eu^{2+} and the left-hand neighboring COT, and r_b is the one between an Eu^{2+} and the right-hand neighboring COT. It is interesting to point out that in the X^- state, $r_a < r_b$, namely, r_a is about 2.1−2.2 and r_b is about 2.4−2.6, while the opposite is true in the A^- state, where r_a is about 2.4−2.6 and r_b is about 2.2. We assumed the polymer $[Eu(COT)]_\infty^-$ takes a single set of the parameters in the X^- state, $r_a(X^-) = 2.181$ and $r_b(X^-) = 2.475$, which are the averaged values of those for $n = 4$. For the A^- state, $r_a(A^-) = 2.454$ and $r_b(A^-) = 2.220$ were assumed in a similar manner.

In Table 1, we summarize the optimized C−C bond distances of the COT ligands in the X^- and A^- states to focus on the geometry of each COT. Here, COT(i) denotes the ith COT counted sequentially from the left in Figure 3 and Eu(i) denotes also the ith Eu from the left. Geometry optimizations for the X^- state with both 4f CORE-A and -B for $n = 1-3$ and with 4f CORE-A for $n = 4$ yielded C_{8v} structures with all of the C−C distances are about 1.42 Å. For the A^- state, the optimizations led to C_{4v} structures, in which only COT(1), with the formal charge of −1, has a largely distorted C_{4v} structure due to the Jahn−Teller effect and has the two kinds of C−C distances of about 1.39 and 1.45 Å, whose average value is again 1.42 Å. We note that, as the position number i increases, the symmetry of COT(i) becomes closer to C_{8v}, reflecting its formal charge of −2. All of the C−H bond distances were 1.09 Å.

We also carried out the frequency analysis for each state of $n = 1-3$ with 4f CORE-A. For $n = 1$ and 2, the optimized geometries for the X^- and A^- states were both stable structures. For $n = 3$, while the X^- state was stable, a doubly degenerate imaginary frequency of 8.89 cm^{-1} was obtained for the A^- state along a lateral motion from the z axis. However, the energy lowering from the C_{4v} structure was only 0.26 cm^{-1}; thus, we used the geometries restricted to the C_{4v} structure for the A^-

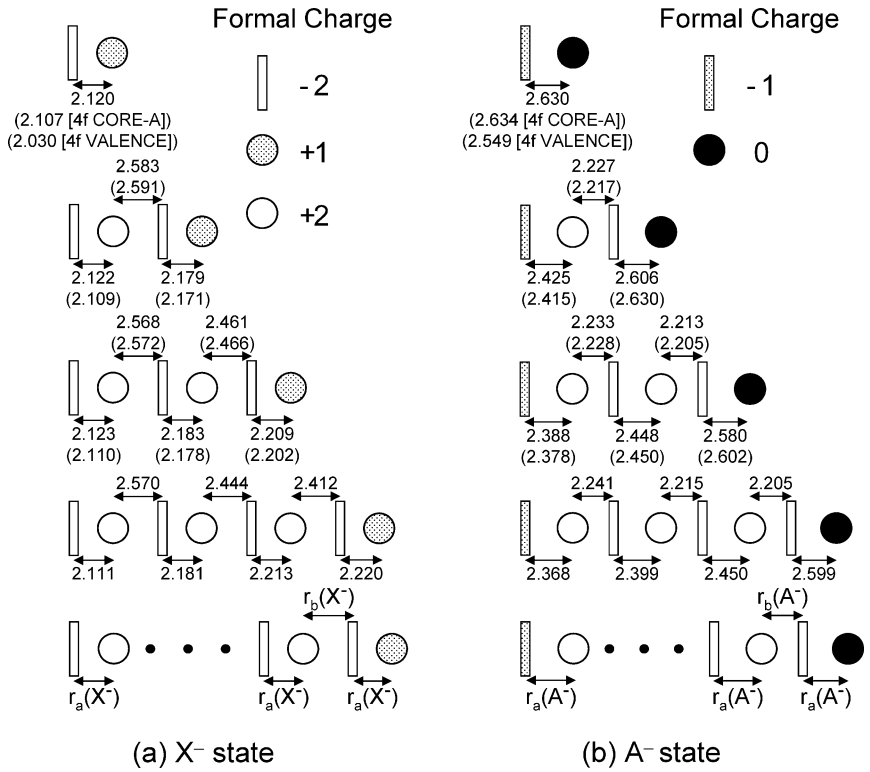

Figure 3. Formal charge distribution and optimized geometry parameters (Å) for the X^- and A^- electronic states of $(n, n)^-$ ($n = 1-4$) calculated by three different treatments. For $n = 1-3$, the optimized parameters of 4f CORE-A and -B are shown, and inside of parenthesis are the parameters of 4f CORE-A. For $n = 4$, optimization was carried out only with the 4f CORE-A. For the X^- and A^- states of $n = 1$, the optimized parameters calculated by 4f VALENCE are also shown. The black, dotted, and white circles denote neutral, +1, and +2 charged metals and dotted and white plates denote −1 and −2 charged COT ligands, respectively. Assumed geometric structures and their parameters for the X^- and A^- states of $[Eu(COT)]_\infty^-$ are $r_a(X^-) = 2.181$, $r_b(X^-) = 2.475$, $r_a(A^-) = 2.454$, and $r_b(A^-) = 2.220$.

TABLE 1: Optimized C−C Bond Distances (Å) of the COTs in the X^- and A^- States[a,b]

$(n, n)^-$	4f CORE	COT(1)	COT(2)	COT(3)	COT(4)
		X^- State			
$(1, 1)^-$	A	1.430			
	B	1.420 (1.419)[c]			
$(2, 2)^-$	A	1.430	1.431		
	B	1.420	1.421		
$(3, 3)^-$	A	1.430	1.431	1.431	
	B	1.420	1.421	1.421	
$(4, 4)^-$	A	1.430	1.431	1.432	1.432
		A^- State[d]			
$(1, 1)^-$	A	1.394 (1.454)			
	B	1.383 (1.444)			
		1.383[c] (1.444)[c]			
$(2, 2)^-$	A	1.397 (1.454)	1.427 (1.433)		
	B	1.386 (1.445)	1.417 (1.423)		
$(3, 3)^-$	A	1.397 (1.455)	1.430 (1.433)	1.430 (1.431)	
	B	1.386 (1.446)	1.419 (1.423)	1.420 (1.421)	
$(4, 4)^-$	A	1.397 (1.455)	1.430 (1.433)	1.432 (1.432)	1.431 (1.431)

[a] For $n = 1-3$, the optimized distances are calculated by the 4f CORE-A and -B, and for $n = 4$, they are calculated only by the 4f CORE-A. [b] COT(i) denotes ith COT counted sequentially from the left in Figure 3. [c] The optimized distances are calculated by the 4f VALENCE. [d] In the A^- state, because of the C_{4v} structure, two kinds of C−C bond lengths are distinctively shown, the longer being in parentheses.

state of $n = 3$ in the following calculations. For $n = 4$, we performed the optimization only with 4f CORE-A, assuming the C_{8v} and C_{4v} structures for the X^- and A^- states, respectively. On the basis of these results, the optimized structures with 4f CORE-B, except for $n = 4$ for which the optimized structure is with 4f CORE-A, will be used for the rest of discussion unless otherwise stated.

To see the charge distribution, we compare the Mulliken charge calculated by 4f CORE-A with the formal charge in Figure 4. Here, we find that formal charges of +2, +1, and 0 of Eu correspond approximately to 0.8, 0.2, and −0.4 of the Mulliken charges, respectively. Similarly, formal charges of −2 and −1 of COT correspond to −1.0 and −0.6 of the Mulliken charges, respectively. Moreover, we notice that this correspondence always holds irrespective of the cluster size and the electronic state. Although the formal charge in the point charge models, to be discussed later, is different from the Mulliken charge quantitatively, it reflects the qualitative tendency of the charge distribution.

Last, in Figure 5, we present the Kohn−Sham orbitals of the highest occupied molecular orbital (HOMO), the second and the third HOMO of $n = 2$ in the X^- state, plotted using the

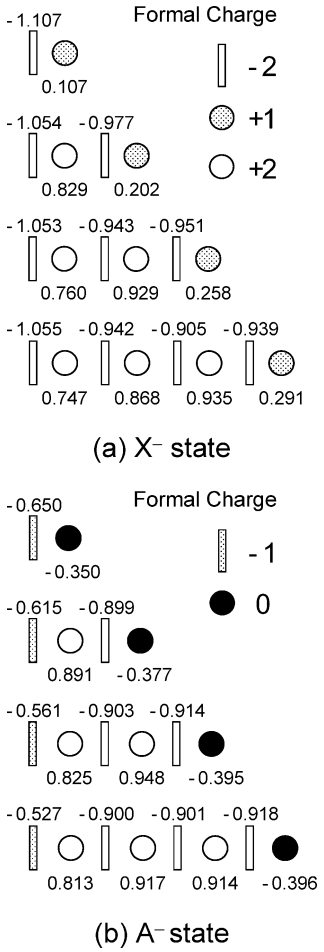

Figure 4. Mulliken population analysis with 4f CORE-A and formal charge distribution for (a) X^- and (b) A^- states of $(n, n)^-$ ($n = 1-4$).

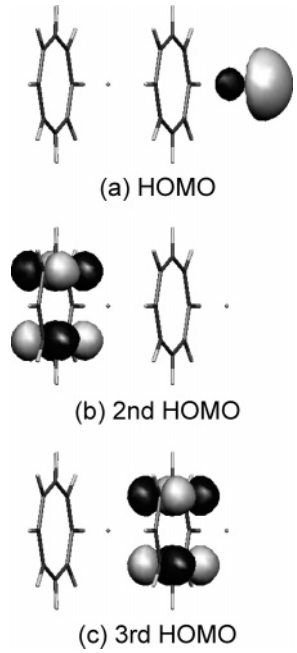

Figure 5. HOMO (a), second (b), third HOMOs (c) for the X^- state of $(2, 2)^-$. Each MO is essentially localized on the Eu atom and COT ligands, respectively.

Molekel program.[44] These orbitals are well localized on each portion; namely, the HOMO is on Eu(2) and the second and the third HOMO are on COT(1) and COT(2), respectively. Note that the latter two orbitals have the same δ symmetry. Interestingly, the HOMO is strongly polarized away from the surrounding COT^{2-} due to its repulsive interaction as also observed in the monohalides of alkali earth and Ln.[45] These characteristics were seen for all of the cluster sizes of $n = 1-4$, both for the X^- and A^- states. On the basis of the orbital localization and ionic charge distribution of $Eu_n(COT)_n^-$, we conclude that these clusters have a strong ionic bonding.

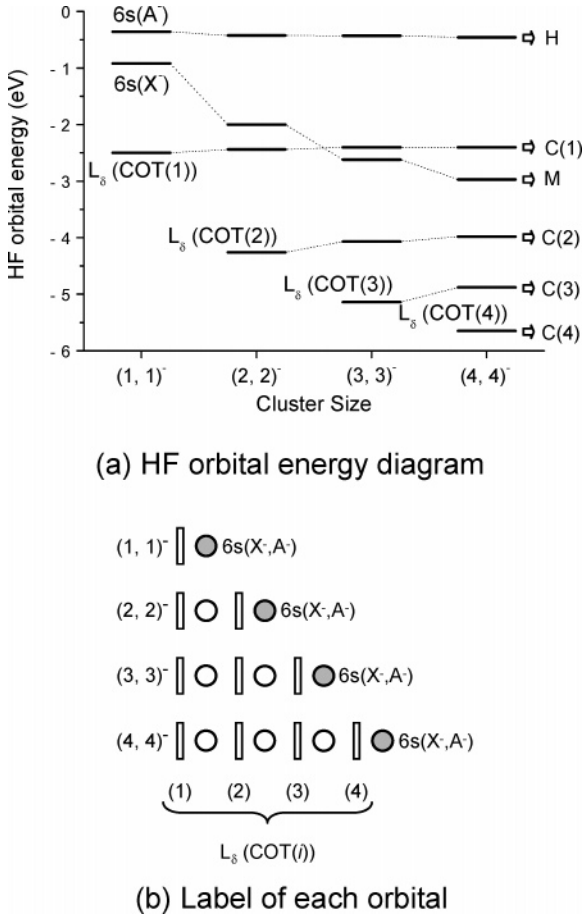

Figure 6. (a) Energy diagram of the valence orbitals (eV) and the corresponding label for detachment peaks. All results are calculated by the UHF method with 4f CORE-B and the optimized distances given in Table 1 and Figure 3. (b) Label of each molecular orbital: 6s(X^-, A^-) denotes the 6s orbital of the terminal Eu in the X^- and A^- states, and L_δ expresses the one of each COT in the X^- state. COT(i) denotes the ith COT counted sequentially from the left in this figure.

4.3. Valence Orbital Energy and VDE. *4.3.1. Hartree−Fock (HF) Orbital Energy.* Before calculating the theoretical VDE, we estimate the valence orbital energies to consider possible detachment channels. For this purpose, the HF orbital energies, which are easily related to VDE with Koompans' theorem, are more meaningful than the Kohn−Sham orbital energies. Thus, we first calculated the unrestricted Hartree-Fock (UHF) orbital energies with 4f CORE-B and summarize their valence orbital energies in Figure 6. Here, 6s(X^-) and 6s(A^-) denote each the 6s orbital of the terminal Eu^+ and Eu in the X^- and A^- states, respectively, and L_δ(COT(i)) denotes the L_δ orbital localized on each COT(i) in the X^- state, as shown in Figure 6b.

We notice that the orbital energy of 6s(X^-) decreases with the cluster size; however, that of 6s(A^-) is almost constant. The energy of L_δ(COT(1)) is almost independent of the cluster size. In addition, in a specific cluster size n, we find that the orbital energy of each L_δ(COT(i)) shows a critical dependence on its position in the clusters; namely, it becomes lower as it goes to

TABLE 2: Comparison of the UHF Orbital Energies Calculated by 4f CORE-B and 4f VALENCE for the X^- State[a,b]

	$(1, 1)^-$			$(2, 2)^-$	
	4f VALENCE	4f CORE-B		4f VALENCE	4f CORE-B
6s(1)	−0.916	−0.929	6s(2)	−2.072	−2.003
L_δ(COT(1))	−2.371	−2.501	L_δ(COT(1))	−2.387	−2.443
L_π(COT(1))	−7.494	−7.587	L_δ(COT(2))	−4.142	−4.257
$4f_\delta(1)$	−9.516		L_π(COT(1))	−7.572	−7.581
$4f_\phi(1)$	−9.620		L_π(COT(2))	−9.266	−9.436
$4f_\pi(1)$	−9.643		$4f_\delta(1)$	−9.512	
$4f_\sigma(1)$	−9.753		$4f_\phi(1)$	−9.550	
			$4f_\pi(1)$	−9.689	
			$4f_\sigma(1)$	−9.709	
			$4f_\sigma(2)$	−11.089	
			$4f_\delta(2)$	−11.109	
			$4f_\phi(2)$	−11.198	
			$4f_\pi(2)$	−11.218	

[a] Calculations on the optimized geometry with 4f CORE-B are shown in Table 1 and Figure 3. [b] COT(*i*) and 4f(*i*) denote orbitals on the *i*th COT and Eu, respectively, counted sequentially from the left in Figure 3.

the right (as the position number *i* increases). In section 4.4, we will reveal the origin of the characteristics of these valence orbital energies.

Further, to investigate the 4f orbital energy and the dependency on the ECPs, we calculated the UHF orbital energies for the X^- state by using 4f VALENCE with the highest spin multiplicities of 9 and 16 for $n = 1$ and 2, respectively. In Table 2, we summarize and compare the 6s, L_δ, L_π, and 4f orbital energies calculated by 4f VALENCE and 4f CORE-B. Despite the different ECPs and basis sets for Eu, we find that the 6s, L_δ, and L_π orbital energies calculated with these two methods are in agreement with each other within a maximum deviation of 0.17 eV.

The orbital energies of 4f in Table 2 are much higher than those of the bare Eu^+ and Eu^{2+} cations due to the strong ligand field by the surrounding COT^{2-}.[46] Moreover, they split to one $4f_\sigma$ and doubly degenerate $4f_\pi$, $4f_\delta$, and $4f_\phi$ components within 0.25 eV in the C_{8v} structure. The magnitude of the splitting pattern of 4f is significantly different from that of the 5f orbitals of actinocenes.[47−49] Because the 5f orbitals are more extensive than the 4f orbitals and their energies are higher than the HOMO (L_δ) of COT, the interactions between the 5f orbitals and COT ligands are much stronger. On the other hand, because the compact 4f orbitals of Ln are lower in energy than that of the inner orbitals of COT, the splitting energies are smaller, and the splitting pattern is expected to depend strongly on their local charge. Although we did not perform any calculations with other spin multiplicities, because of the small splitting energies of the 4f orbitals and the reasonable agreement in the other valence orbital energies, we consider that the 4f shell can be treated as the core, unless the photodetachment of a 4f electron is explicitly examined. In that case, as we will see later, Koopmans' theorem overestimates the VDE very much, and the DFT method including orbital relaxation effects shows much better performance. An interesting point to be added here is that the orbital energies of 4f and L_π also depend on their positions in the clusters. The reason for this dependence is similar to that of L_δ, which we will discuss in section 4.4.

4.3.2. Detachment from 6s(X^-, A^-) and L_δ(COT(1)). Having investigated the valence and 4f orbital energies, we assigned the two detachment channels: first, the M peak to a detachment from 6s(X^-) and, second, the C(1) peak to a detachment from L_δ(COT(1)) as shown in Figures 1 and 6.

Then, we calculated the VDEs for these two channels using the more quantitative ΔDFT method, in which the VDEs were evaluated from the difference in the DFT total energies of $Eu_n(COT)_n^-$ and the corresponding one-electron detached neutral states at the anion equilibrium geometry. First, we investigated the dependency of the calculated VDEs on the three computational methods, 4f CORE-A and -B and 4f VALENCE. We found that the differences between 4f CORE-A and 4f CORE-B for the M and C(1) peaks of $n = 1-4$ are less than 0.1 eV, and those between 4f CORE-B and 4f VALENCE for the two peaks of $n = 1$ are also less than 0.1 eV. Therefore, in the following discussion, we only show the calculation results with 4f CORE-B.

In Figures 1 and 2, we present the calculated VDEs with 4f CORE-B as solid sticks along with the experimental spectra. The calculated values for the two peaks M and C(1) in Figure 1 are in a fair agreement with the experiment at 355 nm. Specifically, they reproduce the characteristic behavior; the first peak shifts to the higher energy side as the cluster size increases, while the second peak is independent of the cluster size.

As for electron detachment from the excited A^- state, two detachment channels are also expected: first, from 6s(A^-) (H peak) and, second, from the COT^{2-} ligands. For each cluster size, we obtained the calculated VDEs for the H peak near 0.9 eV and for the second peak near 3.0 eV. Because this second peak of the A^- state would overlap with the broad C(1) peak of the X^- state, it is experimentally difficult to identify the second peak distinctly from these two peaks. On the other hand, the H peak can be observed clearly for cluster size $n \geq 2$ as in Figure 1. Although the H peak for $n = 1$ might be overlapped with the M peak, the weak peak near 0.9 eV can be assigned to the detachment from 6s(A^-) of the excited A^- state, and its weak intensity reflects an evidence for the minor production of the A^- state. In fact, the intensity ratio between the H and M peaks depended on the source conditions such as stagnation pressure for He carrier gas; the lower stagnation pressure gave the H peak intensity stronger relative to that of the M peak. Note that the H peak becomes prominent with cluster size, which seemingly corresponds to the smaller energy difference between the X^- and A^- states in larger clusters. This point will be discussed further in section 4.5.

4.3.3. Detachment from Each L_δ(COT(i)) Orbital. Next, we consider electron detachment from each L_δ(COT(*i*)) in the X^- state (C(*i*) peak). We calculated the VDEs using the UHF orbital energies in Figure 6 and Koopmans' theorem instead of the ΔDFT method, because the latter method cannot yield excited states with the same symmetry as the lowest state due to the convergence problem practically and the Hohenberg−Kohn theorem conceptually; namely, each state obtained by the electron detachment from these L_δ orbitals belongs to the same symmetry. We compared the results with the experimental spectra taken with the photon energy of 213 nm (5.83 eV) in Figure 2. The calculation also reproduces the characteristic peaks qualitatively. The successive peaks whose number is equal to that of the COTs can be assigned to detachment from each L_δ(COT(*i*)).

4.3.4. Detachment from 4f Orbitals. Let us consider the electron detachment from the 4f orbitals in the X^- state. We found a peak around 3.7 eV in the spectra of both $n = 1$ and $n = 2$ of Figure 2. (That for $n = 2$ appears as a shoulder.) Figure 7 shows the photoelectron spectrum for barium (Ba)−COT cluster anions of $Ba_2(COT)_2^-$ together with that for $Eu_2(COT)_2^-$ at 213 nm. Because a Ba atom has an electron configuration of $[Xe]4f^06s^2$, it is expected that Ba−COT forms an identical

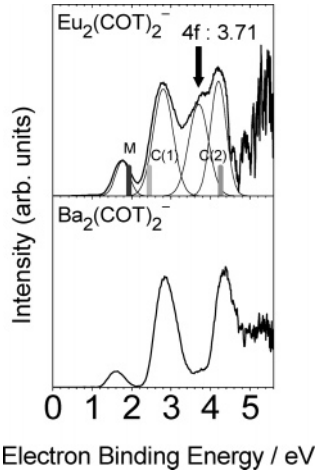

Figure 7. Photoelectron spectrum for $Ba_2(COT)_2^-$ together with that for $Eu_2(COT)_2^-$ at 213 nm. There is apparently an additional photodetachment contribution of 4f orbitals around 3.5−4 eV in the spectra of $Eu_2(COT)_2^-$. The spectral envelopes in the 213-nm spectra were deconvoluted into a set of component Gaussian functions. For $Eu_2(COT)_2^-$ at 213 nm, one additional peak appears at 3.71 eV as labeled by a downward arrow.

sandwich cluster with Eu−COT without 4f electrons, where a Ba atom takes a Ba^{2+} state in the clusters. In fact, the mass distributions of anionic and neutral Ba−COT were very similar to those of Eu−COT; the successive series of (n, $n + 1$), (n, n), and (n, $n - 1$) clusters for Ba−COT appear prominently.[50] The abundance of $Ba_1(COT)_1^-$ was too small to measure the photoelectron spectrum. As expected from the identical ionic distribution between Eu−COT and Ba−COT, both give almost the same EA and similar overall features as shown in Figure 7, while there is apparently an additional photodetachment contribution of 4f orbitals around 3.5−4.0 eV in the spectra of $Eu_2(COT)_2^-$. To assign the position of the electronic transition clearly, the spectral envelopes in the 213-nm spectra were deconvoluted into a set of component Gaussian functions as indicated by the curves in Figure 7. For $Eu_2(COT)_2^-$ at 213 nm, one additional peak appears at 3.71 eV, as labeled by a downward arrow in Figure 7.

With the ΔDFT method, we calculated the final neutral states with one hole in the $4f_\phi(1)$ as the initial guess and obtained VDEs for $n = 1$ and 2 as 4.256 and 4.313 eV, respectively. Especially for $n = 2$, the converged hole state was not localized in 4f(1) but delocalized in both 4f(1) and 4f(2). Therefore, the experimental peak around 3.7 eV is due to a detachment channel from the delocalized 4f orbitals. Because the 4f orbitals are very compact, the detachment of a 4f electron causes a very large shrinking of other outer orbitals and stabilizes the final neutral state significantly. For this reason, the VDE calculated for the detachment of a 4f electron with ΔDFT becomes much smaller than that predicted with Koopmans' theorem given in Table 2. We note that this type of large orbital relaxation upon photoionization from a compact-sized orbital was observed previously in the $(3d_\sigma)^{-1}$ ionization channel of V_nBz_{n+1}.[7] From these results, it seems plausible to assign the peak around 3.7 eV to the $4f^{-1}$ channel, although the photoelectron spectrum for the $Ba_1(COT)_1^-$ cannot be measured.

The source of the difference (about 0.6 eV) between the experimental and calculated VDEs for the $4f^{-1}$ channel is attributable to the ECP or the DFT method, because the ΔDFT method with the 4f VALENCE treatment overestimates the ionization energies for the $4f^{-1}$ channel of the Eu^+ and Eu^{2+} cations by about 1 eV. Therefore, the ΔDFT results for the $4f^{-1}$ channel for $n = 1$ and 2, with an overestimation of about 0.6 eV, are reasonable within this calculation error. For more detailed analyses, it would be necessary to calculate with other theoretical methods. Although this remains as our future study, the detachments from the 6s and COT(i) were not affected very much by the explicit inclusion of 4f orbitals; therefore, we will take a look at the characteristic behavior of these detachments in the next section.

4.4. Point Charge Model. Using the HF orbital energies in Figure 6, we noticed that Koopmans' theorem is able to explain the cluster size dependences of the M, C(i), and H peaks. The variation of the HF orbital energies can be divided into kinetic and potential energy parts. For the relevant valence orbitals, we observed that the kinetic energies showed very weak cluster size dependences, because each molecular orbital is largely localized and does not change its shape significantly. It is, therefore, considered that the origin of the variation of the orbital energy is due to the potential part, especially the intracluster electrostatic potential. Here, we have developed two point charge models reflecting the strong ionic bonding of the $Eu_n(COT)_n$ clusters. In a model, we explicitly treated only the electrons belonging to a metal atom or COT ligand, from which photodetachment takes place, and the remaining Eu metals and COT ligands as point charges distributed as in Figure 3. Then, we performed the DFT calculation for one Eu atom or one COT molecule with the surrounding point charges with the CHARGE keyword in the Gaussian program package and calculated VDEs by the ΔDFT method with thus calculated energies. This method is referred to the "Point Charge + DFT" method.

As another model, using the classical electrostatic formula, we simply evaluated the electrostatic potentials which are created by the surrounding point charges Q_i at $\mathbf{r}_i$, namely,

$$V^a_{\mathrm{class}}(\mathbf{r}) = \sum_{i=1} \frac{Q_i}{|\mathbf{r} - \mathbf{r}_i|} \qquad (1)$$

Here, $\mathbf{r}$ is a position vector at which the potential is evaluated and is the average position of the electron detaching from the orbital a. For $\mathbf{r}_i$, we applied the optimized geometry shown in Figure 3. The electron binding energy is the work to be done on an electron to detach it to infinity. Therefore, the electrostatic potential can be regarded as VDE, and this method is called as the V^a_{class} method. In what follows, these two approximate point charge models provide us with a simple and qualitative explanation for the photoelectron spectra and reveal that the characteristic behavior of the M, C(i), and H peaks originates from the one-dimensional strong ionic bonding.

4.4.1. M Peak. The M peak was assigned to electron detachment from the 6s orbital of Eu^+ in the X^- state ($6s(X^-)$). Therefore, we approximated the remaining Eu^{2+} and COT^{2-} ligands by +2 and −2 point charges, respectively, and placed them along the z axis using the optimized geometry, as shown in Figure 3. Then, we employed the Point Charge + DFT method. As for the $V^{6s(X^-)}_{\mathrm{class}}$ method, considering the spatial extent of $6s(X^-)$ (Figure 5), we took a position $\mathbf{r}$ of the detaching electron at 1.733 Å outside that of Eu^+ for all n. This value of 1.733 Å comes from the expectation value for the position (orbital centroid) of the $6s(X^-)$ electron for $n = 1$.

In the upper part of Figure 8, we show the results obtained by the two point charge models in comparison to other calculation results and experiment. Note that we shift the absolute value of $V^{6s(X^-)}_{\mathrm{class}}$ to fit with the ΔDFT calculation value at $n = 1$. Clearly, the point charge models reproduce other data qualitatively despite their simplicity. Specifically, the asymptotic

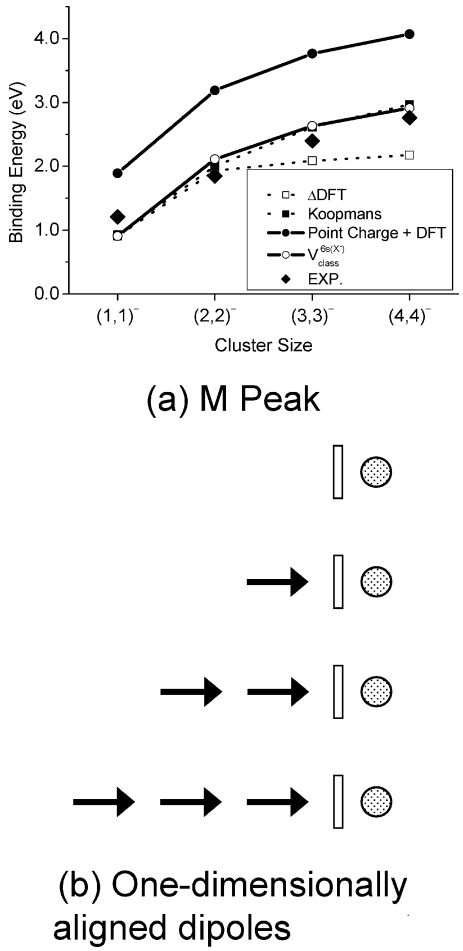

Figure 8. (a) Calculation results of the point charge models for the M peak of $(n, n)^-$ ($n = 1-4$) in comparison with other calculations and experimental data. (b) Schematic diagram for the Coulombic interaction between the detaching electron for the M peak and dipoles which align one-dimensionally in the same direction.

behavior of VDE is well reproduced. Therefore, we conclude that the characteristic behavior of the M peak results from the variation of the electrostatic potential felt by the detaching electron induced by the surrounding Eu^{2+} and COT^{2-} which can be approximated as point charges.

Now, we consider the relation between the cluster size and the variation of the electrostatic potential. As schematically shown in the lower part of Figure 8, viewing from Eu^+, the increase of the cluster size corresponds to the attachment of a pair of $+2$ and -2 point charges to the left side of the cluster: this pair is regarded as an electric dipole. The Eu−COT cluster has the one-dimensional structure so that the dipoles align one-dimensionally in the same direction on increasing the cluster size. Therefore, the increase of the cluster size can be regarded as the stacking of dipoles on the left side of the cluster. Each dipole stabilizes the detaching electron in Eu^+ by an energy that is inversely proportional to the square of the distance between the detaching electron and the attached dipole. The sum of such stabilization energies converges asymptotically to a constant value with *n*. An asymptotic convergence is observed as a characteristic behavior of the M peak and reflects the one-dimensional ionic bonding structure of the $Eu_n(COT)_n^-$ clusters.

4.4.2. C(i) and H Peaks. In a similar manner, we can apply the point charge models to the C(*i*) and H peaks. As mentioned before, the C(1) peak is always assigned to the electron detachment from COT(1) in the X^- state (L_δ(COT(1))), and the H peak is assigned to the detachment from the neutral Eu(*n*)

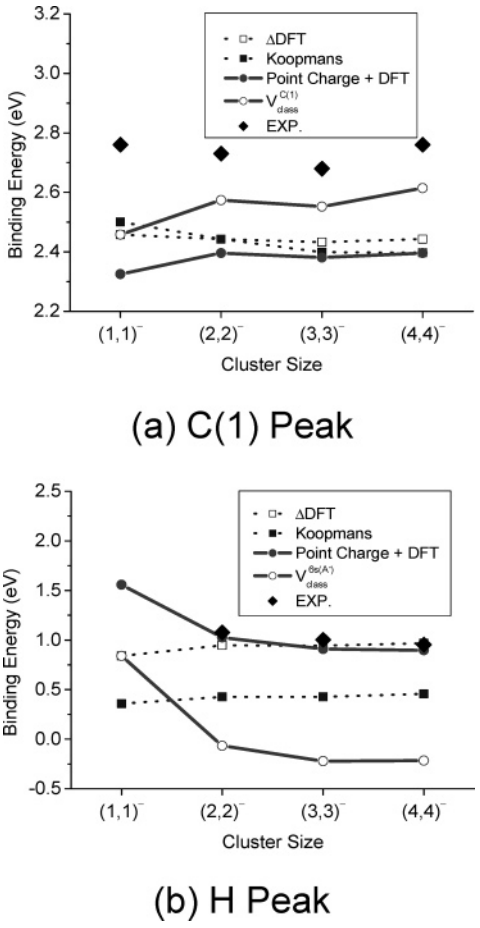

Figure 9. Calculation results of the point charge models for the C(1) (a) and H (b) peaks of $(n, n)^-$ ($n = 1-4$) in comparison with other calculations and experimental data.

in the A^- state ($6s(A^-)$). Moreover, both peaks hardly shift on increasing the cluster size. In applying eq 1 to the C(1) peak, we calculated the value at the center of the COT ring. As for the H peak in the A^- state, a value of 0.844 Å was used as the position of the $6s(A^-)$ centroid. Figure 9 shows the calculated results for the C(1) and H peaks in comparison to other data. The two point charge models also give a qualitative explanation for the size-independent behavior of the C(1) and H peaks. Namely, the electrostatic potentials at the left-end COT(1) in the X^- state and neutral Eu in the A^- state are almost independent of the cluster size.

For the C(1) peak, let us consider the relation between the cluster size and the variation of the electrostatic potential in view of the left-end COT(1) in the X^- state with looking at Figure 3. In this case, the increase of the cluster size corresponds to the change of the right-end Eu^+ to Eu^{2+} and the addition of a pair of COT^{2-} and Eu^+: the attachment of a group of $+1$, -2, and $+1$ point charges to the right side of the cluster. Because this group is regarded as an electric quadruple, the stabilization energy is inversely proportional to the third power of the distance between the detaching electron on COT(1) and the quadruple. Namely, the electrostatic potential at the left-end COT(1) in the X^- state is almost independent of the cluster size in contrast to that at the right-end Eu^+ (M peak).

As for the H peak, a similar explanation can be applied; namely, viewing from the neutral Eu in the A^- state, the increase of the cluster size corresponds to the attachment of a group of -1, $+2$, and -1 point charges, which is approximated as a quadruple, to the left side of the cluster. Therefore, the cluster

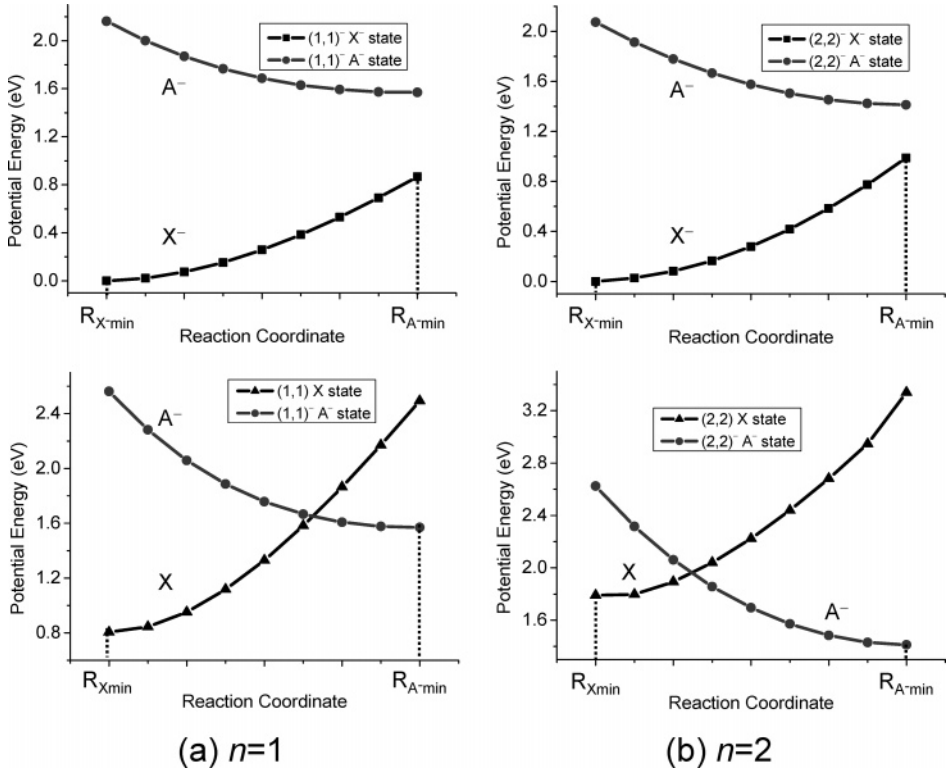

Figure 10. One-dimensional potential curves of the X^- and A^- states along the LST path connecting the minimum structures of these two states for, $n = 1$, 2, and those for the X and A^- states, for $n = 1$, 2.

size dependence of the C(1) and H peaks is much smaller than that of the M peak.

Next, we give a simple explanation for the strong position dependence in the orbital energies of COT(i) and 4f(i) in the X^- state as shown in Figure 6 and Table 2. For example, in the $(3, 3)^-$ cluster, the L_δ orbital energy of COT(2) is about 1.7 eV lower than that of COT(1), and that of COT(3) is about 1.1 eV lower than that of COT(2). Looking at Figure 3 and the lower part of Figure 8, we notice that COT(3) is stabilized by two dipoles consisting of the combination of $(COT(1)^{2-}\ Eu(1)^{2+})$ and $(COT(2)^{2-}\ Eu(2)^{2+})$, while COT(2) is stabilized by only one dipole of $(COT(1)^{2-}\ Eu(1)^{2+})$. Therefore, the orbital energy becomes lower when going to the right because of more stabilization by dipole stackings. A similar explanation is applicable to other cluster sizes so that this gradient among the orbital energies of COT(i) and 4f(i) is also regarded as an interesting characteristic in the one-dimensional ionic bonding cluster.

We should point out that, contrary to the X^- state, the L_δ orbital energies of COT(i) in the A^- state do not show a clear stairs-like behavior in the cluster. This is possibly because the A^- state does not show a clear dipole chain structure, namely, a significant bond alternation, as shown in Figure 3.

On the basis of the above discussion, we estimated each VDE for the polymer $[Eu(COT)]_\infty^-$ using the assumed geometric parameter $r_a(X^-/A^-)$and $r_b(X^-/A^-)$ for the X^- and A^- states, respectively, in section 4.2 and Figure 3. In the calculation, we first accumulated the variation of each VDE from $n = 4$ to $n = \infty$ using eq 1 and, second, added the accumulated variation to the experimental data of $n = 4$. In this way, we extrapolated each VDE empirically to $n = \infty$ and obtained values of 2.894, 2.449, and 0.972 (eV) for the M, C(1), and H peaks, respectively. The VDE for the M peak showed a monotonic convergence, and the difference in the VDE between $n = 30$ and $n = \infty$ was 0.096 eV. On the other hand, those for the C(1) and H peaks converged quickly at $n = 4$.

Similar point charge models have been used for the analyses of, for example, chemical shift in core ionization energies,[51−53] electron affinities and ionization energies,[54,55] solvent effect in the condensed phase,[56,57] and so on. In these cases, the point charge models have been used mainly for analyzing the substituent effects. In this work, the variation of the intracluster electrostatic potential has been studied by increasing the cluster size, and the characteristic behavior of the photodetachment spectra has been analyzed. Similar phenomena are also expected in other clusters with a strong ionic bonding, to which the point charge models can be conveniently applied.

4.5. Relations among the X^-, A^-, and X States. In this last section, we investigate the relative energies among the X^-, A^-, and neutral ground X states to consider the stability of the A^- state. Recently, several groups have suggested that a laser vaporization or pulsed arc method generates clusters in metastable structures.[12,58] Therefore, it is very interesting to look at the energy and structure relations between the X^- and A^- states theoretically. The adiabatic excitation energies from X^- to A^- of $n = 1-4$ were calculated as 1.569, 1.413, 1.384, and 1.382 eV, respectively. To investigate possible relaxation mechanisms from the metastable A^- state, we calculated one-dimensional potential energy curves for the X^- and A^- states of $n = 1$ and 2, as shown in the upper part of Figure 10. Here the potential energy is relative to the minimum energy of the X^- state. R_{X^-min} and R_{A^-min} represent the optimized nuclear structure for the X^- and A^- states, respectively. The reaction path is an artificial one on which all the structural parameters are assumed to change linearly from R_{X^-min} to R_{A^-min} using the LST path[33] in the Cartesian coordinates and was calculated with 4f CORE-B. Clearly, the A^- state is higher in energy than the X^- state at all the coordinates.

We also investigated the relative energy between the A^- and the neutral X states along a similar artificial reaction path between R_{Xmin} and R_{A^-min} and show the potential curves in the lower part of Figure 10. The neutral X state is the final state of

the one-electron detachment from the terminal Eu^+ in the X^- state.[59] As for the A^- and X state potential curves of $n = 1$, we notice that the minimum energy of the A^- state is higher than that of the X state and these potential curves show a crossing; therefore, there is a low barrier on the reaction path from A^- to X. A magnitude of the barrier is only about 600 cm^{-1}. On the other hand, for $n = 2$, the minimum energy of the A^- state is lower than that of the X state and the reaction barrier from R_{A^-min} to R_{Xmin} is about 1 eV which is much larger than that of $n = 1$.

From these calculation results, we can consider two possible relaxation processes from the A^- state: (i) radiative relaxation to the X^- state with fluorescence, $A^- \rightarrow X^- + h\nu$, and (ii) nonradiative autodetachment to the X state, $A^- \rightarrow X + e^-$. In the A^- state, the electronic configurations of the COT^- and neutral Eu metal portions are $L_\sigma^2L_\pi^4L_\delta^3$ and $4f^76s^2$, respectively, and those in the X^- state are $L_\sigma^2L_\pi^4L_\delta^4$ and $4f^76s^1$, respectively, so that process (i) is equivalent to the one-electron transition from the 6s to the L_δ orbital. Because these orbitals have different symmetries of σ and δ with respect to the molecular axis, this σ-to-δ transition is forbidden. Therefore, the radiative relaxation process (i) cannot take place effectively. The process (ii) can be considered as a simultaneous process consisting of an electron transfer from 6s to L_δ and an electron detachment from 6s. The theoretical estimate of such an autodetachment lifetime is possible using, for example, the complex coordinate method,[60] but we can simply discuss the efficiency of the process by comparing the potential curves alone. Note that the autodetachment can take place only in the nuclear configurations where the A^- state is less stable than the X state. Therefore, from the lower part of Figure 10, the autodetachment probability in $n = 1$ is expected to be larger than that in $n = 2$ because the former has a smaller reaction barrier to arrive at the nuclear configurations where the autodetachment becomes possible. In the spectra of $n = 1$ in Figure 1, the H peak is close to the M peak, so that it would be difficult to verify the preparation of the A^- state unambiguously. On the other hand, the small H peaks can be observed in the spectra for the A^- state of $n = 2$ or larger. This experimental observation is consistent with the theoretical analysis above, because once the A^- state is prepared, it relaxes neither to the X^- nor to the X state efficiently and it is stable enough to be detected.

5. Conclusions

In this work, we have studied the geometric and electronic structures of the $Eu_n(COT)_n^-$ anion clusters on the basis of the photoelectron spectra and the DFT method. The geometry optimization for the anions with a 4f core ECP and basis set gave two lower-lying states, the ground-state X^- as a dominant product and the excited-state A^- as a minor product in the experiment, both of which have a one-dimensional structure and strong ionic bonding. The combined experimental and theoretical study made it clear that in the X^- state, the orbital energies of 6s largely decrease with the cluster size and those of the L_δ orbitals on COTs have a stairs-like behavior in the clusters, in which the highest step has an almost constant energy independent of the cluster size. In the A^- state, the 6s level had a negligible cluster size dependence and the L_δ orbitals on COTs showed no stairs-like behavior, in a sharp contrast with that in the X^- state. All this characteristic behavior was interpreted by the position-sensitive intracluster electrostatic potential evaluated by the simple point charge models

To investigate the detachment channels from the 4f orbitals, we measured the photoelectron spectra of Ba−COT and performed the DFT calculation with the 4f valence ECP and basis set. We assigned the peaks of $n = 1$ and $n = 2$ around 3.7 eV to the $4f^{-1}$ channel.

With the point charge models, we were able to estimate the VDE for $[Eu(COT)]_\infty^-$ as 2.894, 2.449, and 0.972 (eV) for the M, C(1), and H peaks, respectively. Such a polymer is interesting as a one-dimensional conductor, because it would have stairs-like orbital energies, and electrical conductivity may arise due to the positively charged soliton generated by electron detachment from the deeper L_δ orbitals.[61] In addition, such polymers may show the characteristic energy transfer behavior due to the dipole chains.[62−64]

Last, we summarized the energetic relations among the X^-, A^-, and X states using the LST paths and concluded that the A^- state can be observed experimentally because of inefficient relaxation processes to the ground X^- and X states. We have recently studied the ionization energies of the X state which also shows size dependence due to the strong ionic bonding and one-dimensional structure.[59]

For the V−Bz cluster, we have previously found a significant cluster size dependence in the valence orbital energies, and their origin was due to the delocalization of the d_δ orbitals of V through the Bz LUMOs. In this study of Eu−COT, we have also found a similar size dependence; however, it was proved to be due to the very strong intracluster electrostatic potential caused by the strong ionic bonding. All of the results indicate that the unique electronic structure of $Eu_n(COT)_n^-$ is due to the one-dimensional structure. In other words, the characteristic feature observed experimentally is a clear evidence of the one-dimensional strong ionic bonding of the clusters.

Acknowledgment. This work was supported in part by Grants-in-Aids for Scientific Research and for the 21st Century COE program "KEIO Life Conjugate Chemistry (LCC)" both from the Ministry of Education, Culture, Sports, Science, and Technology (MEXT), Japan. The authors thank the Research Center for Computational Science, Okazaki National Research Institutes, for the use of the Fujitsu VPP5000, SGI2800, NEC SX-7, and HPC computers.

References and Notes

(1) Dietz, T. G.; Duncan, M. A.; Powers, D. E.; Smalley, R. E. *J. Chem. Phys.* **1981**, *74*, 6511.
(2) Bondybey, V. E.; English, J. H. *J. Chem. Phys.* **1981**, *74*, 6978.
(3) Bondybey, V. E.; English, J. H. *J. Chem. Phys.* **1982**, *76*, 2165.
(4) Geusic, M. E.; Morse, M. D.; O'Brien S. C.; Smalley, R. E. *Rev. Sci. Instrum.* **1985**, *56*, 2123.
(5) Nakajima, A.; Kaya, K. *J. Phys. Chem. A* **2000**, *104*, 176.
(6) Yasuike, T.; Nakajima, A.; Yabushita, S.; Kaya, K. *J. Phys. Chem. A* **1997**, *101*, 5360.
(7) Yasuike, T.; Yabushita, S. *J. Phys. Chem. A* **1999**, *103*, 4533.
(8) Miyajima, K.; Muraoka, K.; Hashimoto, M.; Yasuike, T.; Yabushita, S.; Nakajima, A.; Kaya, K. *J. Phys. Chem. A* **2002**, *106*, 10777.
(9) Pandey, R.; Rao, B. K.; Jena, P.; Blanco, M. A. *J. Am. Chem. Soc.* **2001**, *123*, 3799.
(10) Kandalam, A. K.; Rao, B. K.; Jena, P.; Pandey, R. *J. Chem. Phys.* **2004**, *120*, 10414.
(11) Rayane, D.; Allouche, A. R.; Antoine, R.; Broyer, M.; Compagnon, I.; Dugourd, Ph. *Chem. Phys. Lett.* **2003**, *375*, 506.
(12) Rabilloud, F.; Rayane, D.; Allouche, A. R.; Antoine, R.; Aubert-Frécon, M.; Broyer, M.; Compagnon, I.; Dugourd, Ph. *J. Phys. Chem. A* **2003**, *107*, 11347.
(13) Miyajima, K.; Nakajima, A.; Yabushita, S.; Knickelbein, M. B.; Kaya, K. *J. Am. Chem. Soc.* **2004**, *126*, 13202.
(14) Shumann, H.; Meese-Marktscheffel, J. A.; Esser, L. *Chem. Rev.* **1995**, *95*, 865.
(15) Hayes, R. G.; Thomas, J. L. *J. Am. Chem. Soc.* **1969**, *91*, 6876.
(16) Mares, F.; Hodgson, K.; Streitwieser, A., Jr. *J. Organomet. Chem.* **1970**, *24*, C68.
(17) Ely, S. R.; Hopkins, T. E.; Dekock, C. W. *J. Am. Chem. Soc.* **1976**, *98*, 1624.

(18) Greco, A.; Cesca, S.; Bertolini, W. *J. Organomet. Chem.* **1976**, *113*, 321.
(19) Wayda, A. L.; Mukerji, I.; Dye, J. L.; Rogers, R. D. *Organometallics* **1987**, *6*, 1328.
(20) Hodgson, K. O.; Raymond, K. N. *Inorg. Chem.* **1972**, *11*, 3030.
(21) Hodgson, K. O.; Mares, F.; Starks, D. F.; Streitwieser, A., Jr. *J. Am. Chem. Soc.* **1973**, *95*, 8650.
(22) Dekock, C. W.; Ely, S. R.; Hopkins, T. E.; Brault, M. A. *Inorg. Chem.* **1978**, *17*, 625.
(23) Raymond, K. N.; Eigenbrot, C. W., Jr. *Acc. Chem. Res.* **1980**, *13*, 276.
(24) Xia, J.; Jin, Z.; Chen, W. *J. Chem. Soc., Chem. Commun.* **1991**, 1214.
(25) Dolg, M.; Fulde, P.; Küchle, W.; Neumann, C.-S.; Stoll, H. *J. Chem. Phys.* **1991**, *94*, 3011.
(26) Dolg, M.; Fulde, P.; Stoll, H.; Preuss, H.; Chang, A.; Pitzer, R. M. *Chem. Phys.* **1995**, *195*, 71.
(27) Liu, W.; Dolg, M.; Fulde, P. *J. Chem. Phys.* **1997**, *107*, 3584.
(28) Liu, W.; Dolg, M.; Fulde, P. *Inorg. Chem.* **1998**, *37*, 1067.
(29) Kurikawa, T.; Negishi, Y.; Hayakawa, F.; Nagao, S.; Miyajima, K.; Nakajima, A.; Kaya, K. *J. Am. Chem. Soc.* **1998**, *120*, 11766.
(30) Kurikawa, T.; Negishi, Y.; Hayakawa, F.; Nagao, S.; Miyajima, K.; Nakajima, A.; Kaya, K. *Eur. Phys. J. D* **1999**, *9*, 283.
(31) Miyajima, K.; Kurikawa, T.; Hashimoto, M.; Nakajima, A.; Kaya, K. *Chem. Phys. Lett.* **1999**, *306*, 256.
(32) Hosoya, N.; Takegami, R.; Suzumura, J.; Yada, K.; Koyasu, K.; Miyajima, K.; Mitsui, M.; Knickelbein, M. B.; Yabushita, S.; Nakajima, A. *J. Phys. Chem. A* **2005**, *119*, 9.
(33) Halgren T. A.; Lipscomb, W. N. *Chem. Phys. Lett.* **1977**, *49*, 225.
(34) Nagao, S.; Negishi, Y.; Kato, A.; Nakamura, Y.; Nakajima, A.; Kaya, K. *J. Phys. Chem. A* **1999**, *103*, 8909.
(35) Nakajima, A.; Taguwa, T.; Hoshino, K.; Sugioka, T.; Naganuma, T.; Ono, F.; Watanabe, K.; Nakao, K.; Konishi, Y.; Kishi, R.; Kaya, K. *Chem. Phys. Lett.* **1993**, *214*, 22.
(36) Hotop, H.; Lineberger, W. C. *J. Phys. Chem. Ref. Data* **1975**, *4*, 539.
(37) Becke, A. D. *J. Chem. Phys.* **1993**, *98*, 5648.
(38) Frisch, M. J.; Trucks, G. W.; Schlegel, H. B.; Scuseria, G. E.; Robb, M. A.; Cheeseman, J. R.; Zakrzewski, V. G.; Montgomery, J. A., Jr.; Stratmann, R. E.; Burant, J. C.; Dapprich, S.; Millam, J. M.; Daniels, A. D.; Kudin, K. N.; Strain, M. C.; Farkas, O.; Tomasi, J.; Barone, V.; Cossi, M.; Cammi, R.; Mennucci, B.; Pomelli, C.; Adamo, C.; Clifford, S.; Ochterski, J.; Petersson, G. A.; Ayala, P. Y.; Cui, Q.; Morokuma, K.; Malick, D. K.; Rabuck, A. D.; Raghavachari, K.; Foresman, J. B.; Cioslowski, J.; Ortiz, J. V.; Stefanov, B. B.; Liu, G.; Liashenko, A.; Piskorz, P.; Komaromi, I.; Gomperts, R.; Martin, R. L.; Fox, D. J.; Keith, T.; Al-Laham, M. A.; Peng, C. Y.; Nanayakkara, A.; Gonzalez, C.; Challacombe, M.; Gill, P. M. W.; Johnson, B. G.; Chen, W.; Wong, M. W.; Andres, J. L.; Head-Gordon, M.; Replogle, E. S.; Pople, J. A. *Gaussian 98*, revision A.7; Gaussian, Inc.: Pittsburgh, PA, 1998.
(39) Hammons, J. H.; Hrovat, D. A.; Borden, W. T. *J. Am. Chem. Soc.* **1991**, *113*, 4500.
(40) Wenthold, P. G.; Hrovat, D. A.; Borden, W. T.; Lineberger, W. C. *Science* **1996**, *272*, 1456.
(41) http://www.theochem.uni-stuttgart.de/pseudopotentials/index.en.html.
(42) Dunning, T. H., Jr.; Hay, P. J. In *Modern Theoretical Chemistry*; Schaefer, H. F., III, Ed.; Plenum: New York, 1976; Vol. 3, p 1.
(43) Hehre, W. J.; Ditchfielf, R.; Pople, J. A. *J. Chem. Phys.* **1972**, *56*, 2257.
(44) Flükiger, P.; Lüthi, H. P.; Portmann, S.; Weber, J. *MOLEKEL*, version 4.2; Swiss Center for Scientific Computing: Manno, Switzerland, 2000−2002.
(45) Gotkis, I. *J. Phys. Chem.* **1991**, *95*, 6086.
(46) Field, R. W. *Ber. Bunsen-Ges. Phys. Chem.* **1982**, *86*, 771.
(47) Boerrigter, P. M.; Baerends, E. J.; Snijders, J. G. *Chem. Phys.* **1988**, *122*, 357.
(48) Rösch, N.; Streitwieser, A., Jr. *J. Am. Chem. Soc.* **1983**, *105*, 7237.
(49) Pepper, M.; Bursten, B. E. *Chem. Rev.* **1991**, *91*, 719.
(50) Hosoya, N.; Suzumura, J.; Yada, K.; Takegami, R.; Yabushita, S.; Nakajima, A. *J. Phys. Chem. A*, submitted.
(51) Manne, R. *J. Chem. Phys.* **1967**, *46*, 4645.
(52) Gelius, U.; Heden, P. F.; Hedman, J.; Lindberg, B. J.; Manne, R.; Nordberg, R.; Nordling, C.; Siegbahn, K. *Phys. Scr.* **1970**, *2*, 70.
(53) Basch, H. *Chem. Phys. Lett.* **1970**, *5*, 337.
(54) Gregson, K.; Hall, G. G. *Mol. Phys.* **1969**, *17*, 49.
(55) Nagase, S.; Kobayashi, K. *Chem. Phys. Lett.* **1994**, *228*, 106.
(56) Day, P. N.; Jensen, J. H.; Gordon, M. S.; Webb, S. P.; Stevens, W. J.; Krauss, M.; Garmer, D.; Basch, H.; Cohen, D. *J. Chem. Phys.* **1996**, *105*, 1968.
(57) Day, P. N.; Pachter, R.; Gordon, M. S.; Merrill, G. N. *J. Chem. Phys.* **2000**, *112*, 2063.
(58) Kronik, L.; Fromherz, R.; Ko, E.; Ganteför, G.; Chelikowsky, J. R. *Nat. Mater.* **2002**, *1*, 1.
(59) Takegami, R.; Hosoya, N.; Suzumura, J.; Yada, K.; Nakajima, A.; Yabushita, S. *Chem. Phys. Lett.* **2005**, 403, 169.
(60) Yasuike, T.; Yabushita, S. *Chem. Phys. Lett.* **2000**, *316*, 257.
(61) Skotheim, T. A., Ed. *Handbook of Conducting Polymers*; Marcel Dekker: New York, 1986.
(62) de Leeuw, S. W.; Solvaeson, D.; Ratner, M. A.; Michl, J. *J. Phys. Chem. B* **1998**, *102*, 3876.
(63) Sim, E.; Ratner, M. A.; de Leeuw, S. W. *J. Phys. Chem. B* **1999**, *103*, 8663.
(64) de Jonge, J. J.; Ratner, M. A.; de Leeuw, S. W.; Simonis, R. O. *J. Phys. Chem. B* **2004**, *108*, 2666.